DAS observations and modeling of perforation-induced guided waves in a shale reservoir

Ariel Lellouch[1], Steve Horne[2], Mark A. Meadows[3], Stuart Farris[1], Tamas Nemeth[4], and Biondo Biondi[1]

Abstract

Perforation shots can be recorded by downhole distributed acoustic sensing (DAS) arrays. In this study, we demonstrate that guided waves induced by perforation shots propagate in a low-velocity shale reservoir layer. Such guided waves have a high frequency content of up to 700 Hz and are dispersive, with lower frequencies propagating faster than higher frequencies. They can propagate as P- and S-waves, and their group velocity is higher than their phase velocity. The high temporal and spatial resolution of the DAS array enables unaliased recording despite short wavelengths. The guided waves disappear from the records when the well exits the shale formation. Synthetic modeling predicts their existence for acoustic and elastic cases in simple velocity models. We show that perforation shots from an offset well at a distance of about 270 m can be recorded by the DAS array. Induced guided S-waves undergo significant disturbances while propagating through previously stimulated zones. These disturbances manifest as kinematic and dynamic changes of the recorded wavefield and as scattered events. The nature of the stimulation-induced changes is interpreted as a combination of unknown spatial and temporal effects linked to fluid-filled fractures. Guided waves hold tremendous potential for high-resolution reservoir imaging and should be used in conjunction with conventional DAS arrays and state-of-the-art DAS interrogators.

Introduction

Distributed acoustic sensing (DAS) is an emerging technology that enables continuous spatial and temporal recording of the seismic field by interrogating an optical fiber (Mateeva et al., 2013; Biondi et al., 2017; Lindsey et al., 2017). In addition, DAS can easily tolerate temperature and pressure regimes typically encountered in reservoirs and does not prohibit downhole operations. DAS is used for passive and active surveys in land and marine environments. Newly drilled boreholes are often instrumented with optical fibers that enable multiple applications, such as temperature measurements, vertical seismic profiling surveys, microseismic monitoring, and low-frequency strain measurements (Mateeva et al., 2014; Daley et al., 2016; Karrenbach et al., 2019).

Perforation shots are useful for velocity model calibration (Maxwell, 2014; Hogarth et al., 2017; Lellouch and Reshef, 2019). In this study, we analyze perforation shots recorded by a downhole DAS array (Lellouch et al., 2019). The fiber is installed behind casing along a deviated well drilled into an unconventional shale layer. This well is used for DAS monitoring and production.

Perforation shots are conducted along the horizontal part of the monitor well. We show that these shots generate waves that propagate through the subsurface, reaching distances of more than 500 m from the source. Through synthetic and field-data analysis, we demonstrate that the low-impedance, strongly anisotropic shale formation acts as a waveguide for P- and S-waves. The waveguide allows for the dispersive propagation of high-frequency (up to 700 Hz) events. While guided waves have been previously observed in coal seams (Buchanan, 1976) and crosswell surveys (Krohn, 1992), downhole DAS allows for unprecedented resolution in the analysis of multiple wave types.

In addition, we analyze perforation shots excited from an offset horizontal well located roughly 270 m from the monitor well. Events are reliably recorded at distances of more than 600 m. Since perforations are part of a stimulation program, we can observe propagation differences of P- and S-guided waves between stimulated and undisturbed parts of the shale reservoir. A larger influence on the S-waves is explained by the presence of fluid-filled fractures in the stimulated area. This study sets the stage for high-resolution mapping of fractured reservoirs.

Subsurface properties and acquisition geometry

In this study area, a deviated well was drilled into an unconventional shale formation. In Figure 1a, we show a side view of the well trajectory. The horizontal part of the well spans more than 1.5 km. In addition, we show results of vertical logging in a nearby well. Depths have been manually adjusted. The shale formation is visible in all logs; it is about 15 m thick and located at depths of roughly 1.97–1.985 km at the vertical well location. In Figure 1b, we show logging results recorded in the horizontal part of the well. They display relatively small lateral variation, indicative of the layered geology of the area. In addition, their analysis shows that the well does not break out of the shale formation at any location, which is confirmed by completion logs. Finally, the significant shear-wave splitting shown in Figure 1b indicates strong anisotropy. As a consequence of the layered geology and shale behavior (Sayers, 2005), a vertically transverse isotropy (VTI) approximation of the anisotropic shale is reasonable for this area. The difference between the vertical P-wave velocity (Figure 1a, red) and the horizontal P-wave velocity (Figure 1b, red) is substantial, indicating the strongly anisotropic nature of the shale layer.

The well has been instrumented with DAS fiber cemented behind casing, and it spans a total distance of almost 4 km from the wellhead to the toe (end of the well). The fiber was interrogated

---

[1]Stanford University, Department of Geophysics, Stanford, California, USA. E-mail: ariellel@stanford.edu; sfarris@stanford.edu; biondo@sep.stanford.edu.

[2]Formerly Chevron Energy Technology Company, London, UK. E-mail: hornes@chevron.com.

[3]Chevron Energy Technology Company, San Ramon, California, USA. E-mail: mmeadows@chevron.com.

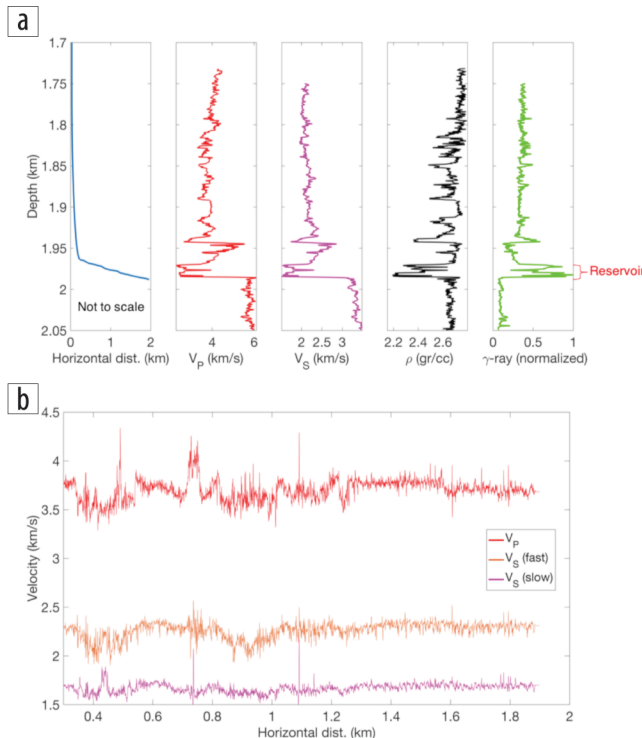[4]Chevron Energy Technology Company, Houston, Texas, USA. E-mail: tamas.nemeth@chevron.com.

Figure 1. (a) Monitor well trajectory (blue) and vertical logging results from a nearby well. Axes are not to scale. We show P- (red) and S- (magenta) wave velocities, density (black), and normalized gamma-ray (green) logs. The shale layer, denoted by a red brace, is located at depths of 1.97–1.985 km and is characterized by low velocities, low density, and high gamma-ray values. (b) Horizontal logs for V_P, fast V_S, and slow V_S in the monitor well. Velocities slightly vary with distance and are nearly constant for the last 900 m. The noticeable discrepancy between fast and slow V_S is associated with shear-wave splitting, indicative of strong anisotropy.
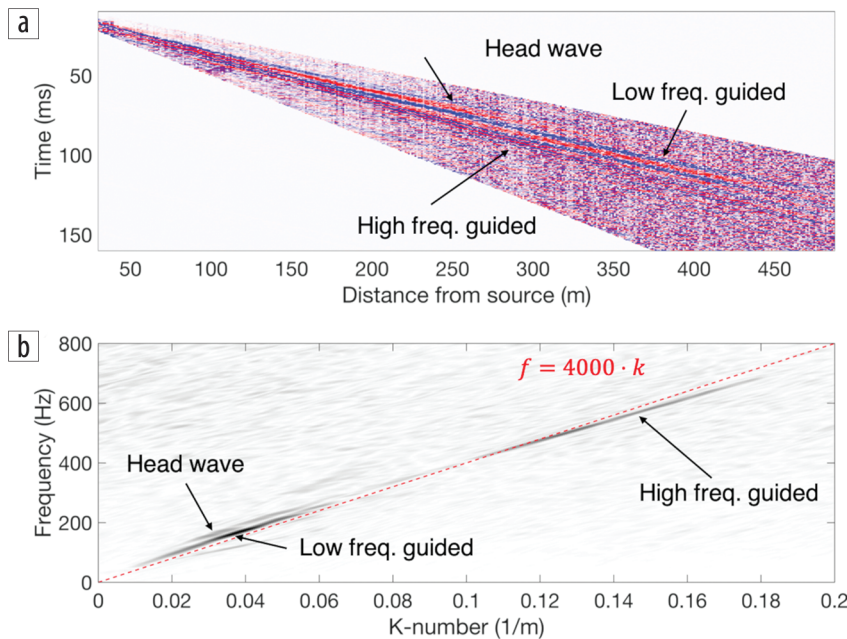

Figure 2. (a) One-sided propagation of a perforation shot and (b) its f-k spectrum. In (b), a linear frequency-wavenumber relation with a propagation velocity of 4 km/s is shown for reference (red dotted line). Events of interest are denoted by black arrows. The shot excites guided waves, which can be seen up to 500 m from the source. They have an extremely high frequency content, reaching up to 700 Hz. Such waves are dispersive, with the lower frequencies propagating faster than the higher ones. In addition, a higher velocity head wave can be observed. It propagates for shorter distances with a lower frequency content than the guided waves and with a velocity that matches that of the layer above the shale formation.

using the Silixa iDAS system, with a channel spacing of 1 m, gauge length of 10 m, and sampling frequency of 2 kHz. Data are acquired as strain rate along the direction of the fiber. Perforation shots are generated as part of a stimulation program. There are 31 stimulation stages along the horizontal part of the DAS-instrumented monitor well, each consisting of five or six perforation shots. Stages start at the toe and are nearly uniformly spaced along the well. The average distance between shots is 10–12 m. Shots are directional and activated 180° from the fiber.

Recorded perforation shot

In Figure 2a, we show a perforation shot initiated roughly 600 m from the toe and associated one-sided propagation toward the heel (the bent part of the well) in the undisturbed area of the reservoir. Different perforation shots are similar to each other and display the same behavior. We apply a velocity filter of 2500–5000 m/s. The f-k analysis of these data is shown in Figure 2b. There are two types of waves in this record that are discernable in both plots — guided waves and head waves. The head wave propagates up to distances of 300 m; it has a frequency content of up to 250 Hz and a velocity that matches that of the layer above the shale formation. There are no clear signs of a head wave from below the shale layer, which has a significantly higher velocity (greater than 5.5 km/s) and impedance contrast than the layer above (see Figure 1a). The guided waves propagate to longer distances (500 m) than the head wave and have a wide frequency content of up to 700 Hz. They are dispersive, with the lower frequencies propagating faster than higher frequencies. This can be observed in temporal records (Figure 2a) and their f-k spectrum (Figure 2b). The lower frequencies generally lie above the dotted line in Figure 2b, while the higher frequencies are below it. In addition, for all frequencies, the phase velocity (f/k) is higher than the group velocity ($\partial f/\partial k$), as expected. As a rough estimate, the phase velocities are higher by about 10%–15%, depending on the frequency.

Synthetic example — Acoustic propagation

In this section, we confirm the existence of guided waves in a simplified acoustic scenario. Figure 3a shows a summary of the synthetic setup. Due to the strong anisotropy of the shale layer, logging velocities have to be adjusted to reasonably match actual propagation velocities. We use vertical logs to build a 1D profile of the P-wave velocity. With such a structure, it is possible to model the vertical/deviated and the horizontal parts of the well in the same medium. P-wave velocities above and below the shale layer are coarsely blocked with constant values. Within the shale area, indicated by high gamma-ray values, we scale the velocities and retain the original

log variations. After scaling, velocities should be close to the average horizontal log velocity. Due to the strong anisotropy of the shale reservoir, such scaling amounts to a 30%–40% increase of the P-wave log velocity. Since the guided waves propagate mostly horizontally in the shale layer, this is a reasonable compromise. Density logs are used directly. Modeled data are shown in Figure 3b, and their *f-k* analysis is shown in Figure 3c. Data are converted to their strain-rate equivalent by using a combination of their spatial and temporal derivatives and applying a spatial filter emulating the 10 m gauge length with which the field data are recorded. For simplicity, we use a rectangular filter, which is only a coarse approximation. Finally, a band-pass filter is applied to match the frequencies of the field data.

We are able to recreate the behavior of guided waves with this simple acoustic model. The dispersion behavior is similar to what we see in the field-data records. However, we observe only a single guided mode in the field data. In the synthetic data, higher order modes are also present. It is worth noting that frequency notches are introduced by the gauge-length effect (Dean et al., 2017). Field data also appear to have notches at the same wavenumbers observed in the synthetic data. A second difference is that the head wave from the top of the layer is absent in the modeled data. We show later that such a head wave arises when elastic modeling is conducted. For a more intuitive understanding of the propagation mechanism, we show two snapshots of the full wavefield in Figure 4. The waveguide nature of the shale layer is evident. In addition, Figure 4 shows the weakness of the head waves when recorded by an array located within the shale layer.

Recording in the nonhorizontal section of the well

In Figure 5, we show records of a perforation shot close to the heel of the well. This shot is recorded by the horizontal and vertical/bending parts of the DAS array. We compare the recorded field data (Figure 5b) with synthetic seismograms (Figure 5a). The depth of the well at different locations is plotted on top of the recorded data. The synthetic wavefield is displayed at the locations where field data were acquired. Distances from the source are computed as Euclidean distance between source and receiver and do not take into account true propagation paths in the nonhorizontal section. In field and synthetic data sets, the guided waves disappear when the well exits the shale formation. This reconfirms that the existence of these waves is limited
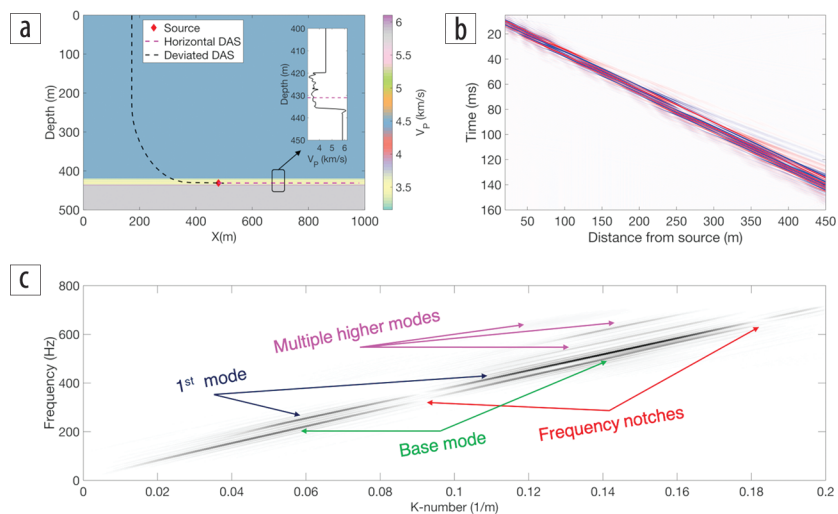

Figure 3. (a) Synthetic example setup. The 1D velocity model is shown in the inset along with a zoomed-in version around the shale reservoir. Velocities above and below the shale are constant. The source is denoted by a red diamond. There are two acquisition setups: horizontal (magenta line) and deviated (black line). The latter follows the true well trajectory near the heel. (b) Data are modeled for horizontal DAS recording and (c) their *f-k* spectrum. Events of interest are denoted by arrows in different colors.
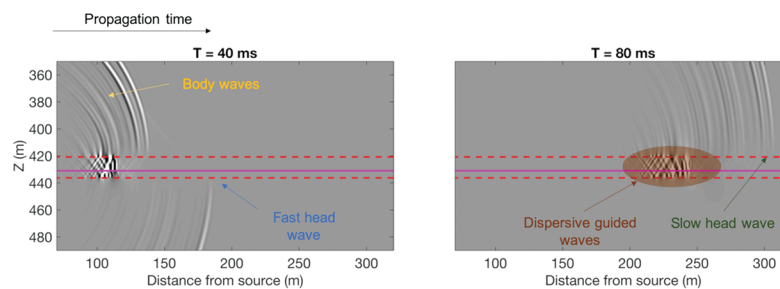

Figure 4. Two snapshots of recorded acoustic data (prior to conversion to strain rate) at 40 and 80 ms after source activation (zoomed in on the shale layer). The magenta line indicates the location of the horizontal recording array. Dashed red lines indicate the boundaries of the shale formation. We denote body waves (yellow), head waves (fast in blue, slow in green) and the dispersive guided waves (brown).

to low-impedance areas within the shale layer. Outside this area, only body waves can propagate. In addition, both records show a clear moveout change when the well exits the shale layer. As the waves continue propagating to the left, they appear to be faster than guided waves propagating to the right, and they decrease in amplitude. This is expected, as propagation outside the shale layer is that of body waves within a faster medium. After analyzing the data from all available perforation shots, we did not see an area within the horizontal section in which the guided waves disappear. This is confirmed by the completion log, according to which the well did not break formation at any location.

The field data display significant S-waves in the nonhorizontal section. Their prominence is due to fiber directivity, which is more sensitive to S-wave polarizations in this geometrical setup (Martin, 2018). The S-waves appear to follow a different moveout pattern than the P-waves, indicating variable V_P/V_S as confirmed by the vertical logs (Figure 1). Of course, the acoustic modeling results in Figures 3–5 do not contain S-waves, providing motivation for a further modeling study with elastic wave propagation.
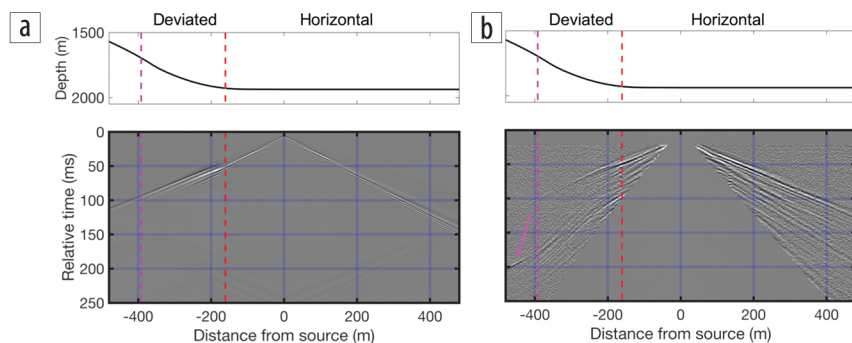
Figure 5. (a) Synthetic and (b) field records close to the heel of the well. The well's depth profile is plotted on top of records. The dashed red line indicates where the well exits the formation. The dashed magenta line is located where the well is vertical. Seismograms are ordered by signed distance and computed as a 2D Euclidean source-receiver distance. At the location where the well exits the formation, the guided waves disappear, and first arrivals undergo a clear moveout change. Propagation outside the shale reservoir is faster, as expected. For the field-data record, S-waves are clearly visible in the vertical part of the well (magenta arrow).
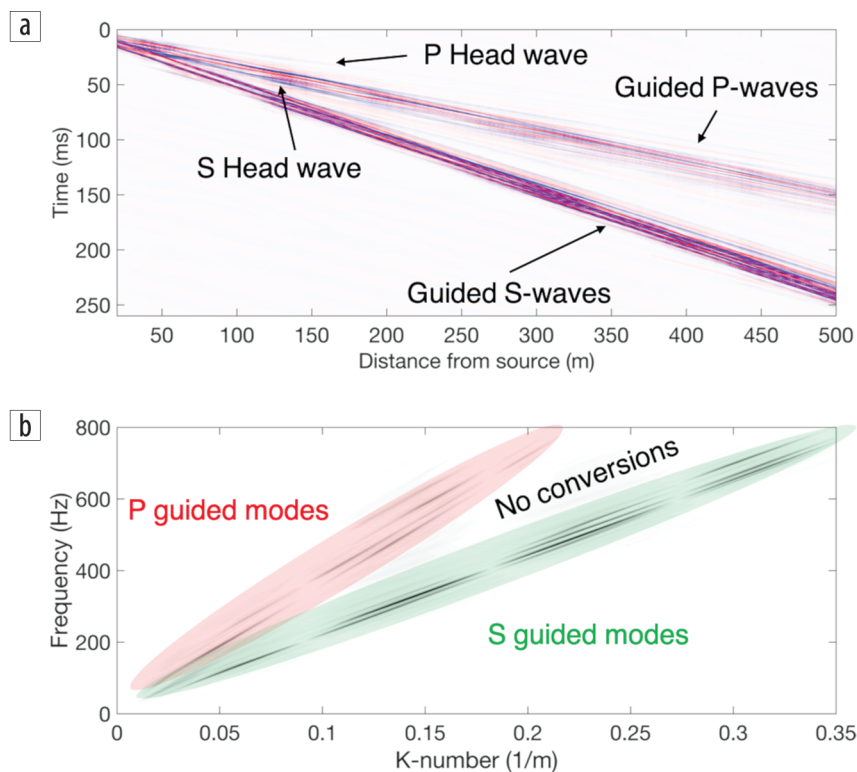

Figure 6. Elastic modeling for horizontal acquisition. Recorded data are in (a) and their *f-k* analysis is in (b). The P head wave from the top of the layer is visible and denoted by an arrow. In addition, the S head wave is visible. Also shown are P- and S-waves that propagate as dispersive guided waves, containing multiple modes. They are denoted in red and green, respectively, in (b). Note that guided S-waves are stronger than guided P-waves. Interestingly, there do not seem to be any propagating PS/SP converted modes. If they existed, they would appear between the P- and S-modes, roughly where "no conversions" is marked in the *f-k* domain.

Synthetic example — Elastic propagation

In the field data, S-waves are significantly weaker than P-waves. In addition, they appear clearly only for certain shots. We recompute 2D synthetic seismograms for a horizontal acquisition geometry using the isotropic elastic wave equation. The perforation shot is modeled as a force stress source directed along the z axis and perpendicular to the horizontal array. Data are extracted as displacements in the x-axis direction and converted to strain-rate equivalents. Construction of the S-wave velocity

model is similar to the P-wave modeling workflow discussed earlier, but scaling is performed to match the fast S-waves. As a result, if guided waves can propagate in such a model, they will also exist for the slower S-waves.

Modeled data and their *f-k* analysis are shown in Figure 6. The head wave arising from the P-waves can now be clearly seen in accordance with the field-data records. There is also an S head wave, propagating at the shear velocity of the medium below the shale. Both head waves propagate for short distances, as is the case for the field data. P- and S-guided waves propagate with a dispersive behavior containing multiple modes, as in the acoustic case. As before, slower frequencies propagate faster than high frequencies, and the phase velocity is higher than the group velocity. It is worth mentioning that there are no clear conversions between P- and S-waves. If there were, converted events should have a moveout between that of the P- and S-waves, but that area in the *f-k* domain remains empty. Guided waves propagate with supercritical angles in the shale layer. At such angles (above 70°), the Zoeppritz equations (Aki and Richards, 2002) predict small conversion coefficients. Naturally, the complexity of the subsurface may add other degrees of freedom and frequency-dependent behavior.

In contrast to the modeling results, P-waves are stronger in field data. In addition, S-waves are only visible for some of the perforation shots. This effect is due to the used source mechanism. There are better representations for a perforation shot than the directional force source. We tested the approach given by Fehler and Pearson (1984), which yielded results that are in agreement with the field data. Nevertheless, the synthetic results we show prove that the shale layer can sustain guided S-waves.

Recording of perforation shots from a parallel well

Perforation shots were also excited in a nearby offset well and recorded by the monitor well. The horizontal sections of the wells are approximately parallel and separated by a distance of 270 m. The perforation shots are part of a stimulation program, going from toe to heel and separated into stages. Each stage consists of five perforation shots spaced roughly 10 m apart. The distance between stages is about 50 m, and there is a 6- to 8-hour delay

between consecutive stages. As a result, for each recorded shot we can observe propagation through previously stimulated zones (toward the toe) as well as undisturbed zones (toward the heel).

In Figure 7, we show the analysis of a perforation shot located roughly 500 m from the toe. The recorded data display P- and S-guided waves, with the previously observed dispersion effect of faster propagation at the lower frequencies. A reasonable approximation of the traveltimes for a given frequency component can be obtained using a constant velocity, which is strong evidence of the 1D nature of the velocity structure. The S-wave velocity indicates that propagation corresponds to the fast S-mode (Figure 1), or SH-mode in the case of VTI anisotropy. Data undergo offset binning with 0.25 m resolution in order to create a uniformly sampled version of the data for f–k analysis. The frequency content is again high and reaches up to 700 Hz for the P-waves and 600 Hz for the S-waves. The f–k analysis also shows that, as before, phase velocities are higher than group velocities for all frequencies. In contrast to perforation shots excited in the monitor well, the S-waves are stronger than the P-waves. This validates the elastic synthetic example, showing that the geologic structure can sustain strong S-wave guided modes.

We also observe obvious propagation differences in the previously stimulated and undisturbed parts of the shale reservoir. In the stimulated area, S-waves induce a strong scattered event, visible along a wide portion of the DAS array. The P-arrivals also induce such an event, originating at the same spatial location, but it is much weaker. For many perforation shots, P-induced scattering is invisible, and S-induced scattering is less obvious than in the shot displayed in Figure 7. However, regarding the S-waves, there is a clear disturbance in the propagation of the guided waves, and the record is asymmetric. This property is true for all of the shots we observed. Therefore, we conclude that there is a subsurface heterogeneity, probably caused by a previous stimulation.

In Figure 8, we show a different type of analysis. We observe a 200 m section of DAS channels recording perforation shots from different locations. This is a form of common-receiver gather. H indicates the horizontal distance between shot locations and the center of the common subsurface area that is being analyzed. It is important to remember that there is also a significant time
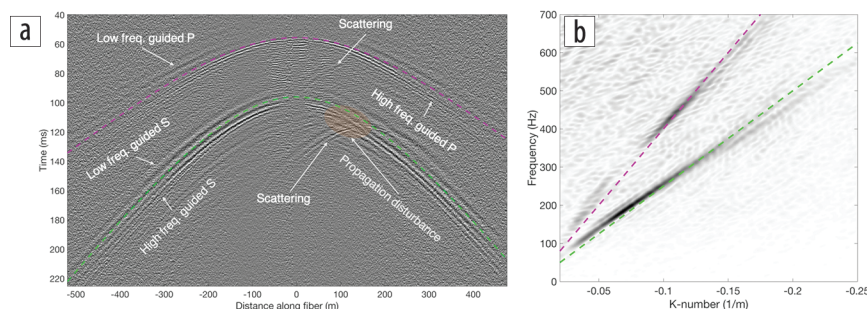

Figure 7. (a) Perforation shot from an offset well. Recorded traces are ordered by 1D signed horizontal distance from the estimated source location. Positive distances (right side of [a]) indicate propagation in the direction of a previously stimulated area. Hyperbolic moveouts, computed with $V_P = 4$ km/s (magenta) and $V_S = 2.5$ km/s (green), are overlaid on recorded data. The absolute timing of the shot is unknown, and the time axis is arbitrary. The dispersive nature of P- and S-waves is clearly visible, as low frequencies propagate faster than higher ones. In addition, we observe a propagation disturbance for the S-waves in the previously stimulated zone (orange ellipse). There is also a scattered event originating at the same location. Such scattering is also present for the P-waves, despite being significantly weaker. (b) f–k analysis of undisturbed propagation (left side of [a]). Two $f = c \cdot k$ lines are plotted, with $c = 4$ km/s (P in magenta) and $c = 2.5$ km/s (S in green).
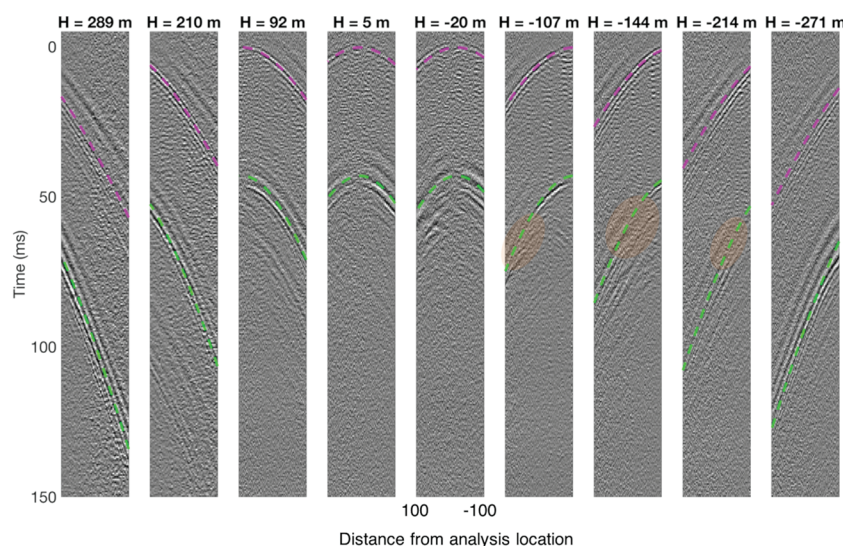

Figure 8. Common-receiver area analysis of different perforation shots. A fixed portion of the DAS array, 200 m wide and recording different perforation shots is displayed. The horizontal 1D distance between the center of the portion of the recording array and the estimated shot location (H) is plotted at the top. Positive distances indicate that the wavefields are propagating in an undisturbed area, whereas negative distances specify propagation through a previously stimulated zone. Hyperbolic moveouts, computed with $V_P = 3.7$ km/s (magenta) and $V_S = 2.3$ km/s (green), are overlaid on recorded data. As the absolute timing of the shot is unknown, the time axis has been manually adjusted. Areas of disturbed S-wave propagation in which P-waves appear as weakly or not affected are marked with ellipses.

difference between shots, as stages are 6 to 8 hours apart. A single shot was chosen from each stage. Propagation in the undisturbed part (H = 289 m, 210 m, and 92 m) appears continuous and smooth for P- and S-events. The perforation shot almost directly in front of the array (H = 5 m) appears disturbed in P- and S-arrivals. We can also observe a polarity flip due to fiber directivity. For H = –20 m, both phases appear disturbed, even though the S is more affected. For propagation in the disturbed part at intermediate distances (H = –107 m and –144 m), we see an interesting phenomenon. The P-arrivals appear practically unaffected, whereas the S-waves are strongly disturbed. In addition, the S-waves appear to generate some scattered energy, propagating in the opposite direction. For H = –214 m, there is no visible scattering, but the propagation is affected for the rightmost part of the

array. At a longer distance (H = –271 m), the wavefront propagation reverts to its undisturbed state.

Discussion

The temporal and spatial resolution offered by DAS systems enables unprecedented recording of high-frequency guided waves. Their spatial wavelength can be as short as 5 m for P-waves and 3 m for S-waves. No feasible conventional acquisition system could sample such wavelengths over a wide range of angles without strongly aliasing them. The wide frequency content of these guided waves confirms the need for temporal sampling at 2 kHz and above. However, in this study the acquisition used a gauge length of 10 m, which interfered with the recorded signal. Newer DAS systems can offer shorter gauge lengths without compromising the signal-to-noise ratio. From this study, it seems that a reduction of the gauge length to 2 or 3 m would be beneficial, especially for S-waves.

The clearest difference due to propagation through previously stimulated areas appears in the S-waves. The greater sensitivity of S-waves to fractures relative to P-waves is a well-known phenomenon (Schoenberg and Sayers, 1995). As part of the reservoir stimulation, we attribute the effect to fluid-filled fractures. S-waves are more easily recorded by DAS fibers in wells adjacent to the treatment well than in the treated well itself. This is due to the favorable geometry of obliquely incident S-wave polarizations arriving from the treatment well. For the same reason, perforation shots excited in the monitor well appear to generate weaker recorded S-wave energy, and the existence of such waves is less consistent from shot to shot. When perforations are recorded from an offset well, S-waves are dominant, and changes in their character can be easily detected. Unquestionably, stimulation induces changes in the subsurface, but uncertainty remains regarding the effect of such changes on time-dependent S-wave behavior. When sources are far enough (greater than 300 m) from the analyzed area, the wavefronts behave as if propagating in an undisturbed medium. This can be explained by two different mechanisms, possibly in combination. The first is that induced fractures close down, and the surrounding matrix returns to its original state (Karrenbach et al., 2019) after a relatively short period, usually over a few hours (Meadows and Winterstein, 1994). The total stimulation time period covered in this study is over several days. The second possible cause is purely spatial, for cases where the extent of the fractures that propagate toward the monitor well is limited. As a result, waves excited at greater distances from the monitor well simply do not cross the disturbed areas.

Due to their high frequency content, guided waves are ideal candidates for high-resolution mapping or imaging of shale reservoirs. We have begun studying their potential for full-waveform inversion by using perforation shots excited at the DAS-equipped well (Biondi et al., 2019). They show signs of high sensitivity to small changes in the velocity model, as expected. Since perforation shots are densely excited, a full-waveform-inversion approach can be used to detect lateral velocity variations and possibly link them to reservoir properties. The S-waves in the crosswell data may, for example, be used in a simple kinematic inversion. Estimating velocity changes

due to previous stimulation may help define the stimulated volume. However, fracture behavior is time dependent, and not all recorded data can be used simultaneously. In addition, accurate source and receiver locations are required.

Conclusions

We show the existence (using field and synthetic data) of P- and S-guided waves induced by perforation shots propagating in a shale reservoir. They disappear when the well exits the formation. These waves are excited whether the perforation shot is conducted in the monitor well or in an offset well. However, the relative strength of P- and S-waves, both of which can propagate in the low-impedance shale layer, varies between the two cases. Guided waves have a high frequency content (up to 700 Hz) and can only be sampled thanks to the spatial and temporal resolution of the DAS array. They are dispersive, with slower frequencies propagating faster than higher ones and with phase velocities that exceed group velocities. By studying perforation shots induced from an offset well, we observe noticeable propagation disturbances in wavefields traveling through stimulated zones. The effect of the induced fractures on S-waves is significant, while in most cases P-wave propagation is weakly, if at all, disturbed. We interpret this as a result of the existence of fluid-filled fractures to which S-waves are more sensitive. The short wavelengths of the guided waves make them ideal candidates for high-resolution mapping of fractured reservoirs. We strongly advocate for the utilization of guided waves in conjunction with state-of-the-art DAS systems in further studies of such areas. **TLE**

Data and materials availability

Data associated with this research are confidential and cannot be released.

Corresponding author: ariellel@stanford.edu

References

Aki, K., and P. G. Richards, 2002, Quantitative seismology: University Science Books.

Biondi, B., A. Lellouch, E. Biondi, and S. Farris, 2019, SEP reports (177), Can we image guided waves by elastic full waveform inversion?, http://sep.stanford.edu/doku.php?id=sep:research:reports, accessed 25 September 2019.

Biondi, B., E. Martin, S. Cole, M. Karrenbach, and N. Lindsey, 2017, Earthquakes analysis using data recorded by the Stanford DAS array: 87th Annual International Meeting, SEG, Expanded Abstracts, 2752–2756, https://doi.org/10.1190/segam2017-17745041.1.

Buchanan, D. J., 1976, The propagation of attenuated SH channel waves: Geophysical Prospecting, **26**, no. 1, 16–28, https://doi.org/10.1111/j.1365-2478.1978.tb01575.x.

Daley, T. M., D. E. Miller, K. Dodds, P. Cook, and B. M. Freifeld, 2016, Field testing of modular borehole monitoring with simultaneous distributed acoustic sensing and geophone vertical seismic profiles at Citronelle, Alabama: Geophysical Prospecting, **64**, no. 5, 1318–1334, https://doi.org/10.1111/1365-2478.12324.

Dean, T., T. Cuny, and A. H. Hartog, 2017, The effect of gauge length on axially incident P-waves measured using fibre optic distributed vibration sensing: Geophysical Prospecting, **65**, no. 1, 184–193, https://doi.org/10.1111/1365-2478.12419.

Fehler, M., and C. Pearson, 1984, Cross-hole seismic surveys: Applications for studying subsurface fracture systems at a hot dry rock geothermal site: Geophysics, **49**, no. 1, 37–45, https://doi.org/10.1190/1.1441559.

Hogarth, L. J., C. M. Kolb, and J. H. Le Calvez, 2017, Controlled-source velocity calibration for real-time downhole microseismic monitoring: The Leading Edge, **36**, no. 2, 172–178, https://doi.org/10.1190/tle36020172.1.

Karrenbach, M., S. Cole, A. Ridge, K. Boone, D. Kahn, J. Rich, K. Silver, and D. Langton, 2019, Fiber-optic distributed acoustic sensing of microseismic, strain and temperature during hydraulic fracturing: Geophysics, **84**, no. 1, D11–D23, https://doi.org/10.1190/geo2017-0396.1.

Krohn, C. E., 1992, Cross-well continuity logging using guided seismic waves: The Leading Edge, **11**, no. 7, 39–45, https://doi.org/10.1190/1.1436887.

Lellouch, A., B. Biondi, S. Horne, M. A. Meadows, and T. Nemeth, 2019, DAS observation of guided waves in a shale reservoir generated by perforation shots: 89th Annual International Meeting, SEG, Expanded Abstracts, 943–947, https://doi.org/10.1190/segam2019-3212667.1.

Lellouch, A., and M. Reshef, 2019, Velocity analysis and subsurface source location improvement using moveout-corrected gathers: Geophysics, **84**, no. 3, KS119–KS131, https://doi.org/10.1190/geo2018-0517.1.

Lindsey, N. J., E. R. Martin, D. S. Dreger, B. Freifeld, S. Cole, S. R. James, B. L. Biondi, and J. B. Ajo-Franklin, 2017, Fiber-optic network observations of earthquake wavefields: Geophysical Research Letters, **44**, no. 23, 11792–11799, https://doi.org/10.1002/2017GL075722.

Martin, E. R., 2018, Passive imaging and characterization of the subsurface with distributed acoustic sensing: PhD thesis, Stanford University.

Mateeva, A., J. Lopez, J. Mestayer, P. Wills, B. Cox, D. Kiyashchenko, Z. Yang, W. Berlang, R. Detomo, and S. Grandi, 2013, Distributed acoustic sensing for reservoir monitoring with VSP: The Leading Edge, **32**, no. 10, 1278–1283, https://doi.org/10.1190/tle32101278.1.

Mateeva, A., J. Lopez, H. Potters, J. Mestayer, B. Cox, D. Kiyashchenko, P. Wills et al., 2014, Distributed acoustic sensing for reservoir monitoring with vertical seismic profiling: Geophysical Prospecting, **62**, no. 4, 679–692, https://doi.org/10.1111/1365-2478.12116.

Maxwell, S., 2014, Microseismic imaging of hydraulic fracturing: Improved engineering of unconventional shale reservoirs: SEG, https://doi.org/10.1190/1.9781560803164.

Meadows, M. A., and D. F. Winterstein, 1994, Seismic detection of a hydraulic fracture from shear-wave VSP data at Lost Hills Field, California: Geophysics, **59**, no. 1, 11–26, https://doi.org/10.1190/1.1443523.

Sayers, C. M., 2005, Seismic anisotropy of shales: Geophysical Prospecting, **53**, no. 5, 667–676, https://doi.org/10.1111/j.1365-2478.2005.00495.x.

Schoenberg, M., and C. M. Sayers, 1995, Seismic anisotropy of fractured rock: Geophysics, **60**, no. 1, 204–211, https://doi.org/10.1190/1.1443748.